

The role of coherent structures in subgrid-scale energy transfer within the log layer of wall turbulence

V. K. Natrajan and K. T. Christensen^{a)}

Department of Theoretical and Applied Mechanics, Department of Mechanical and Industrial Engineering, University of Illinois at Urbana-Champaign, Urbana, Illinois 61801

(Received 10 January 2006; accepted 25 April 2006; published online 14 June 2006)

The present effort documents the relationship between dominant subgrid-scale energy transfer events and coherent motions within the log layer of wall turbulence. Instantaneous velocity fields in the streamwise–wall-normal plane of a zero-pressure-gradient turbulent boundary layer acquired by particle-image velocimetry at $Re_\tau \equiv u_* \delta / \nu = 2350$ are spatially filtered to generate an ensemble of resolved-scale velocity fields in the spirit of large-eddy simulation. The relationship between subgrid-scale dissipation and embedded coherent structures is then studied using instantaneous realizations and conditional averaging techniques. This analysis reveals that strong forward- and backward-scatter events occur spatially coincident to individual hairpin vortices and their larger-scale organization into vortex packets. In particular, large-scale regions of forward scatter are observed along the inclined interface of the packets, coincident with strong ejections induced by the individual vortices. The most intense forward-scatter events are found to occur when these ejections are opposed by sweep motions. Strong backward scatter of energy is observed at the trailing edge of the vortex packets and weaker backscatter is also noted locally around the individual heads of the hairpin structures. The collective observations presented herein demonstrate that hairpin vortices and their organization into larger-scale packets are important contributors to interscale energy transfer in the log layer of wall turbulence. © 2006 American Institute of Physics.

[DOI: [10.1063/1.2206811](https://doi.org/10.1063/1.2206811)]

I. INTRODUCTION

Many recent studies support the existence of hairpin vortices in the outer layer of wall turbulence ($y^+ \equiv y/y_* > 100$, where y_* is the viscous length scale). For clarity, the term *hairpin* is used to broadly refer to vortical structures consistent with symmetric or asymmetric canes, horseshoes, omegas, hairpins, and modified versions thereof. Smith¹ reported the existence of hairpin vortices at low Reynolds number (Re) and suggested an organized alignment of these structures in the streamwise direction. The computations of Zhou *et al.*,^{2,3} in which the evolution of an initial hairpin-like structure was studied in the mean turbulent field of a low- Re channel flow via direct numerical simulations (DNS), revealed a similar organization as well as processes by which these vortices can regenerate from existing structures. At higher Re , Head and Bandyopadhyay⁴ reported the existence of groups of hairpin structures at the outer edge of a zero-pressure-gradient turbulent boundary layer inclined slightly away from the wall. More recently, the work of Adrian *et al.*⁵ established the existence of hairpin vortices and an organized alignment of these structures, termed hairpin vortex packets, throughout the outer layer of a turbulent boundary layer. Their particle-image velocimetry (PIV) measurements in the streamwise–wall-normal plane revealed large-scale hairpin packets characterized by a series of hairpin vortices advecting in the streamwise direction at similar speeds whose heads form an interface inclined away from the wall at a shallow

angle (12° – 20°) and a region of momentum deficit enveloped beneath the interface due to the collective induction of the vortices in a packet. In addition, the recent experiments of Kim and Adrian⁶ indicate that individual hairpin vortex packets may coherently align with one another, forming very-large-scale motions that contain a majority of the kinetic energy and have streamwise extents well exceeding the outer length scale of the flow.

The statistical significance and the role that these large-scale structures play in turbulent transport have also been assessed. Christensen and Adrian⁷ found that estimates of the conditionally averaged velocity field given the presence of a spanwise vortex core (the head of a hairpin) yielded the statistical signature of a typical hairpin vortex packet with streamwise-aligned swirling motions inclined away from the wall at angles consistent with the observations of Adrian *et al.*⁵ Marusic⁸ showed that the long streamwise tail of the two-point spatial correlation of streamwise velocity is attributable to outer-layer vortex organization. These observations provide further evidence that vortex organization is a dominant feature of the outer layer. With regard to transport, Liu *et al.*⁹ found that large-scale motions having length scales on the order of the channel half-height can be reconstructed with only a few low-order proper orthogonal decomposition (POD) modes. These low-order modes contained half of the turbulent kinetic energy and over two-thirds of the Reynolds shear stress in the outer region. These results, complemented by the work of Ganapathisubramani *et al.*,¹⁰ indicate that large-scale motions may dominate turbulent transport in all regions except the very near-wall layer. However, the exact

^{a)}Electronic mail: ktc@uiuc.edu

role that these structures play in interscale energy transfer, a process crucial to proper turbulence modeling, remains unclear.

In a wall-bounded turbulent flow, like channel flow or a turbulent boundary layer, the ratio of the largest to the smallest length scales can be approximated by the friction Reynolds number, $Re_\tau \equiv \delta/y_*$, where δ represents the channel half-height or the boundary-layer thickness. As such, DNS of wall turbulence, in which all dynamically relevant scales are resolved, become impractical at higher Re_τ due to the growing range of scales that must be resolved. To overcome such issues, large-eddy simulation (LES) is a technique often employed for high-Re simulations wherein the larger scales are resolved completely while the smaller scales are modeled in a deterministic manner. (For detailed reviews of LES, the reader is directed to Rogallo and Moin,¹¹ Meneveau and Katz,¹² and Piomelli and Balaras.¹³) The LES governing equations are derived by applying a filter to the Navier-Stokes equations, where the characteristic width of the filter defines the boundary between the resolved (larger) and unresolved (smaller) scales. The filtered continuity and momentum equations are then

$$\frac{\partial \tilde{u}_i}{\partial x_i} = 0 \quad (1)$$

and

$$\frac{\partial \tilde{u}_i}{\partial t} + \tilde{u}_j \frac{\partial \tilde{u}_i}{\partial x_j} = -\frac{1}{\rho} \frac{\partial \tilde{p}}{\partial x_i} + \nu \frac{\partial^2 \tilde{u}_i}{\partial x_j \partial x_j} - \frac{\partial \tau_{ij}}{\partial x_j}, \quad (2)$$

where $\tilde{(\cdot)}$ represents a filtered quantity and τ_{ij} is the subgrid-scale (SGS) stress tensor and embodies the influence of the smaller scales on the evolution of the resolved scales. (This form of the filtered momentum equation assumes the use of a homogeneous filter that permits commutation of the derivative and filtering operators.) The SGS stress tensor is therefore a by-product of the filtering operation and is given by

$$\tau_{ij} = \widetilde{u_i u_j} - \tilde{u}_i \tilde{u}_j. \quad (3)$$

In most cases, the smaller scales are considered to be isotropic, containing a relatively small fraction of the total kinetic energy, which permits their parameterization in terms of a deterministic model that mimics their average interaction with the resolved scales. The implications of discarding the unresolved scales can be clarified by considering the transport equation for the resolved kinetic energy, $\tilde{q}^2 = \tilde{u}_k \tilde{u}_k$,

$$\begin{aligned} \frac{\partial \tilde{q}^2/2}{\partial t} + \tilde{u}_j \frac{\partial \tilde{q}^2/2}{\partial x_j} = & -\frac{1}{\rho} \frac{\partial \tilde{u}_j \tilde{p}}{\partial x_j} - \frac{\partial \tilde{u}_i \tau_{ij}}{\partial x_j} + \nu \frac{\partial^2 \tilde{q}^2/2}{\partial x_j \partial x_j} \\ & - \nu \frac{\partial \tilde{u}_i}{\partial x_j} \frac{\partial \tilde{u}_i}{\partial x_j} - \varepsilon_{\text{sgs}}, \end{aligned} \quad (4)$$

where $\varepsilon_{\text{sgs}} = -\tau_{ij} \tilde{S}_{ij}$ is termed the SGS dissipation (and \tilde{S}_{ij} is the filtered strain-rate tensor) and represents the interscale energy transfer associated with the interaction of the resolved and unresolved scales.¹⁴ Positive values of ε_{sgs} represent energy transfer from the resolved to the unresolved scales and are therefore referred to as forward-scatter events. In contrast, negative values of ε_{sgs} represent energy transfer from

the smaller to the larger scales and are termed backscatter events. In general, the mean SGS dissipation is positive, consistent with the well-accepted notion of a turbulent energy cascade from the larger, energy-containing motions to the smaller, dissipative scales. However, it should be noted that backscatter events can contribute significantly to the net SGS dissipation which, if inadequately modeled, could generate erroneous accumulation or dissipation of resolved-scale kinetic energy.¹⁴ Therefore, SGS models must accurately reproduce energy transfer both to and from the unresolved scales. Unfortunately, many commonly used LES models, like eddy-viscosity models, are purely dissipative and hence can only account for forward scatter of energy.

The fidelity of LES models is commonly assessed through *a priori* testing, which usually involves comparing statistics of modeled SGS parameters to those obtained using fully resolved experimental or DNS data.¹⁵ Data from a DNS has the advantage of being fully resolved from the largest to the dissipative scales (see Refs. 16–18, for example); however, DNS is necessarily limited to low-Re and canonical geometries. In contrast, spatially well-resolved experimental data can be acquired at Reynolds numbers and in complex geometries that are currently inaccessible by DNS and are therefore used frequently to assess the performance of LES models (see Refs. 19–22, among others). While *a priori* statistical comparisons of modeled to true SGS parameters has received considerable attention in the literature, the relationship between embedded coherent motions and the complex transfer of energy across the filter scale in LES has received considerably less attention (see Refs. 21, 23, and 24, for example), particularly in wall turbulence. Based on conditionally averaged flow fields obtained using the variable-interval-spatial-averaging (VISA) technique, Hartel *et al.*²⁵ concluded that energy transfer from the unresolved to the resolved scales in the near-wall region of wall turbulence is often accompanied by strong shear layers characteristic of intense bursting events. Piomelli *et al.*²⁶ used low-Re DNS of turbulent channel flow to study the role of coherent structures in SGS energy transfer and concluded that near-wall turbulent structures are often accompanied by regions of forward and backward scatter occurring in close proximity to one another. Finally, the recent sonic anemometry experiments of Carper and Porte-Agel²⁷ in the atmospheric boundary layer provide detailed evidence linking local interscale energy transfer to three-dimensional (3D) coherent structures. They used conditional averaging methods to show that vortical structures consistent with hairpin vortices are closely associated with localized SGS energy transfer.

The goal of the present effort is to characterize the role that hairpin vortices, and their larger-scale organization into vortex packets, play in interscale energy transfer within the log layer of wall turbulence. PIV measurements in the streamwise-wall-normal plane of a zero-pressure-gradient turbulent boundary layer are used in concert with conditional averaging techniques to study the energy-transfer characteristics of these structures at Reynolds numbers and in a wall-bounded flow that is currently inaccessible by DNS.

TABLE I. Summary of experimental parameters.

Re_τ	δ (mm)	u_* (m/s)	y_* (μm)	No. of vectors per field	No. of realizations
2350	103.1	0.36	43.9	34 776	2500

II. EXPERIMENTS

The analysis presented herein utilizes a large ensemble of two-dimensional (2D) velocity (u, v) fields acquired by PIV in the streamwise-wall-normal (x - y) plane of a turbulent boundary layer by Wu and Christensen.²⁸ As such, only the necessary experimental details are presented and the reader is directed to Ref. 28 for further information. The boundary-layer measurements were made in a low turbulence, open-circuit boundary layer wind tunnel under zero-pressure-gradient conditions. This facility has a documented turbulence intensity of 0.16% in the free stream and the boundary layer develops over a 6.1-m-long hydraulically smooth flat plate that has an elliptically shaped leading edge.²⁹ The friction velocity, u_* , and the viscous length scale, $y_* = \nu/u_*$, were assessed using the Clauser chart method.

Two-thousand five-hundred statistically independent instantaneous velocity realizations were acquired at $Re_\tau \equiv u_* \delta / \nu = 2350$ (equivalently the Karman number) with a field of view of $\delta \times \delta$ and a spatial resolution of $24y_*$ in both spatial directions. This spatial resolution is adequate enough to resolve the vortical structures germane to this study.^{28,30} Standard two-frame cross-correlation methods were used to analyze the PIV images with 50% overlap to satisfy Nyquist's criterion and the time delay between images was chosen to minimize the relative velocity measurement error to less than 1%. Table I summarizes the flow parameters for the experiment.

III. FILTERING AND CALCULATION OF SGS QUANTITIES

In order to study the role that log-layer structure plays in SGS energy transfer, the instantaneous PIV velocity fields are spatially filtered using a filtering operation given by

$$\tilde{f}(\mathbf{x}) = \int_D f(\mathbf{x}') G(\mathbf{x}, \mathbf{x}') d\mathbf{x}', \quad (5)$$

where D is the domain defined by the PIV field of view and G is a filter function. While inhomogeneous filters are normally required in actual LES of wall turbulence due to the inhomogeneity of the wall-normal direction, a one-dimensional (1D) homogeneous filter is employed herein in the homogeneous streamwise direction. As discussed in Völker *et al.*,³¹ wall-normal filtering introduces issues of treatment of continuity and also a commutation error. Further, Porte-Agel *et al.*³² and Tong *et al.*³³ showed that while the filter dimension affects the magnitude of SGS quantities, it does not alter their overall significance or behavior. Therefore, the use of a homogeneous filter in the streamwise direction in the present analysis is deemed sufficient for study-

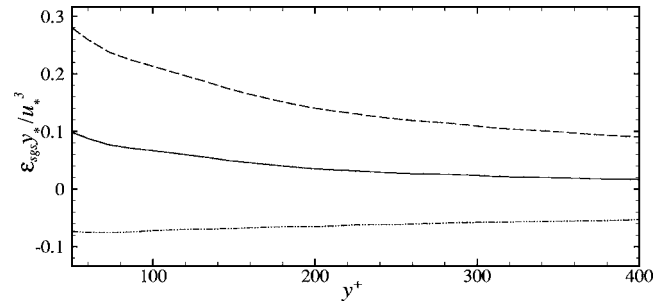


FIG. 1. Mean SGS dissipation, estimated using Eq. (7), as a function of wall-normal position. ---: forward scatter; - · - ·: backscatter; —: net dissipation.

ing the qualitative relationship between SGS energy transfer and embedded coherent motions.

A top-hat filter of the form

$$G(x) = \begin{cases} 1/\Delta & \text{if } |x| < \Delta/2, \\ 0 & \text{otherwise,} \end{cases} \quad (6)$$

is utilized in the present effort with a characteristic filter width of $\Delta = 0.08\delta$, which lies within the inertial subrange of the streamwise spectra of both the streamwise and wall-normal velocities. This filtering operation is performed independently on the streamwise and wall-normal velocity components (u, v) in each instantaneous velocity realization, yielding ensembles of instantaneous resolved-scale velocity fields (\tilde{u}, \tilde{v}). While this filter width may seem severe, the use of a large filter width is consistent with what one might employ in an actual LES of high-Re wall turbulence, like the recent LES of turbulent channel flow reported by Völker *et al.*³¹ Finally, multiple top-hat filter widths within the inertial subrange and a Gaussian filter were also tested and the results presented herein are found to be qualitatively insensitive to both the type and width of the filter.

As noted in the introduction, energy transfer between the resolved and unresolved scales assumes the form of a SGS dissipation, $\epsilon_{\text{sgs}} = -\tau_{ij} \tilde{S}_{ij}$, in the transport equation of the resolved-scale kinetic energy and embodies contributions from six distinct SGS stress-filtered strain-rate products. However, the present planar and 2D PIV fields only allow direct computation of the in-plane components of the SGS stress and filtered strain-rate tensors. Therefore, an estimate of the SGS dissipation given by

$$\epsilon_{\text{sgs}}^{2D} = -(\tau_{11} \tilde{S}_{11} + 2\tau_{12} \tilde{S}_{12} + \tau_{22} \tilde{S}_{22}), \quad (7)$$

is computed. Figure 1 presents the mean SGS dissipation computed using Eq. (7) versus the wall-normal position in the log layer. The mean forward- and backward-scatter contributions to the net SGS dissipation are also shown for comparison. As expected, although the net SGS dissipation is positive, indicative of a net energy transfer from the large to small scales, there exists a significant backscatter contribution to the net SGS dissipation that must be accounted for in the formulation of robust LES models. This backscatter contribution to the net SGS dissipation is also clearly evident in the probability density function (pdf) of ϵ_{sgs} at $y = 0.15\delta$ (Fig. 2). While the forward-scatter tail is longer than that of the

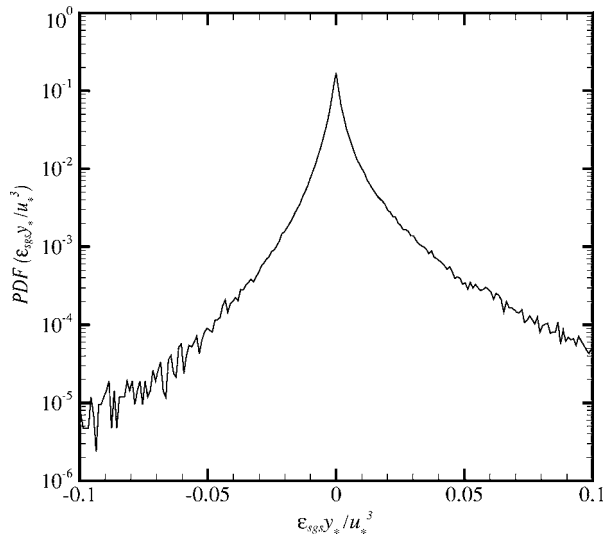


FIG. 2. Probability density function of ε_{sgs} , estimated using Eq. (7), at $y=0.15\delta$.

backscatter, this pdf further illustrates the not insignificant role that backscatter plays in the overall energy transfer across the boundary of the resolved and unresolved scales. In addition, the wall-normal trends noted in Fig. 1 and the qualitative nature of the pdf shown in Fig. 2 are consistent with those reported by Piomelli *et al.*²⁶ in low-Re channel flow, lending support to the 2D approximation of ε_{sgs} utilized herein.

To further justify the use of a 2D estimate of ε_{sgs} , five streamwise-wall-normal planes from a DNS of turbulent channel flow at $\text{Re}_\tau=940$ (Ref. 34) are used to compare the true SGS dissipation calculated using all SGS stress-filtered strain-rate products with the 2D estimate given by Eq. (7). Figure 3 presents a scatter plot of $\varepsilon_{\text{sgs}}^{2D}$ and ε_{sgs} at $y=0.15\delta$

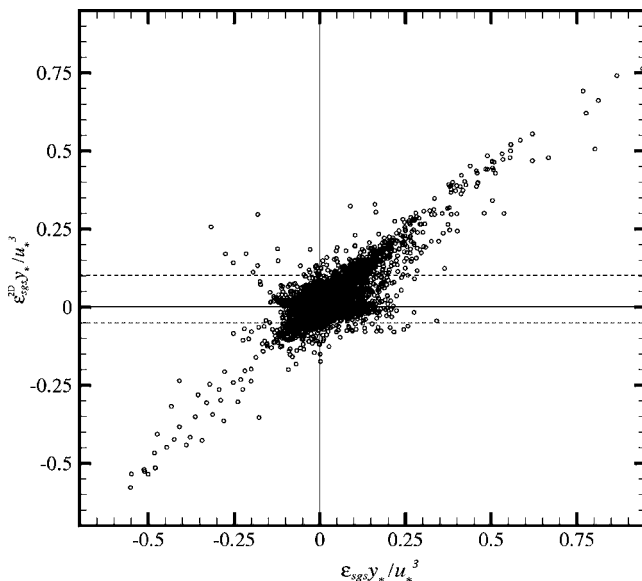


FIG. 3. Comparison of true SGS dissipation with the 2D estimate given by Eq. (7) using data from a DNS of turbulent channel flow at $\text{Re}_\tau=940$ (Ref. 34). The horizontal dashed lines demarcate the forward and backward scatter thresholds imposed in the present analysis.

computed from the DNS data. A vast majority of points, most notably the strongest energy-transfer events, are found to lie in the first and third quadrants, meaning that true forward- and backward-scat events are correctly predicted by $\varepsilon_{\text{sgs}}^{2D}$. Further, nearly all of the erroneously estimated forward- and backward-scat events in the second and fourth quadrants are clustered near zero. Therefore, in order to ensure that such incorrectly estimated forward- and backward-scat events are not included in the present analysis, a threshold is imposed to classify the dissipation at each grid location as a true backscatter event ($\varepsilon_{\text{sgs}} < \varepsilon_t^b$) or a forward-scat event ($\varepsilon_{\text{sgs}} > \varepsilon_t^f$). Results presented herein are for the case where ε_t^b and ε_t^f are chosen to be the mean values of backscatter and forward-scat events, respectively. Since this mean varies with wall-normal location (Fig. 1), so too does the threshold. The dashed horizontal lines in Fig. 3 demarcate the values of the forward- and backward-scat thresholds at $y=0.15\delta$, illustrating that the incorrect 2D estimates in the second and fourth quadrants of the scatter plot are eliminated under this thresholding methodology. The use of this condition ensures that only the correctly identified forward and backward scatter events are considered for statistical computations and minimizes any decorrelation by weak, insignificant, and incorrect 2D estimates of dissipation events. Based upon this classification scheme, the instantaneous SGS dissipation at each grid location is denoted by an event Φ such that

$$\Phi(\mathbf{x}) = \begin{cases} \phi^f = \varepsilon_{\text{sgs}} & \text{if } \varepsilon_{\text{sgs}} > \varepsilon_t^f \text{ for forward scatter,} \\ \phi^b = \varepsilon_{\text{sgs}} & \text{if } \varepsilon_{\text{sgs}} < \varepsilon_t^b \text{ for backscatter,} \\ 0 & \text{otherwise.} \end{cases} \quad (8)$$

For reference, the use of a threshold in this context is not without precedence as Piomelli *et al.*²⁶ utilized a similar methodology for isolating the most significant energy transfer events in their low-Re DNS work. Further, the results presented are found to be qualitatively independent of the threshold, as thresholds ranging from a small fraction to four times the mean have been tested.

IV. INSTANTANEOUS EVIDENCE

In order to assess the role that hairpin vortices and their large-scale organization into vortex packets play in interscale energy transfer, these structures must be effectively visualized in the instantaneous velocity realizations. Galilean decomposition through the removal of a fixed advection velocity from an instantaneous velocity field represents one method for uncovering vortices traveling at this velocity. This identification method is consistent with the definition of a vortex offered by Kline and Robinson:³⁵ “A vortex exists when instantaneous streamlines mapped onto a plane normal to the core exhibit a roughly circular or spiral pattern, when viewed in a frame of reference frame moving with the center of the core.” Galilean decomposition is particularly well suited for visualizing the local flow patterns induced by vortical structures, although it is limited since one must remove a broad range of advection velocities to reveal all of the embedded structure. Alternatively, one can identify vortices in a Galilean-invariant manner through analysis of the local

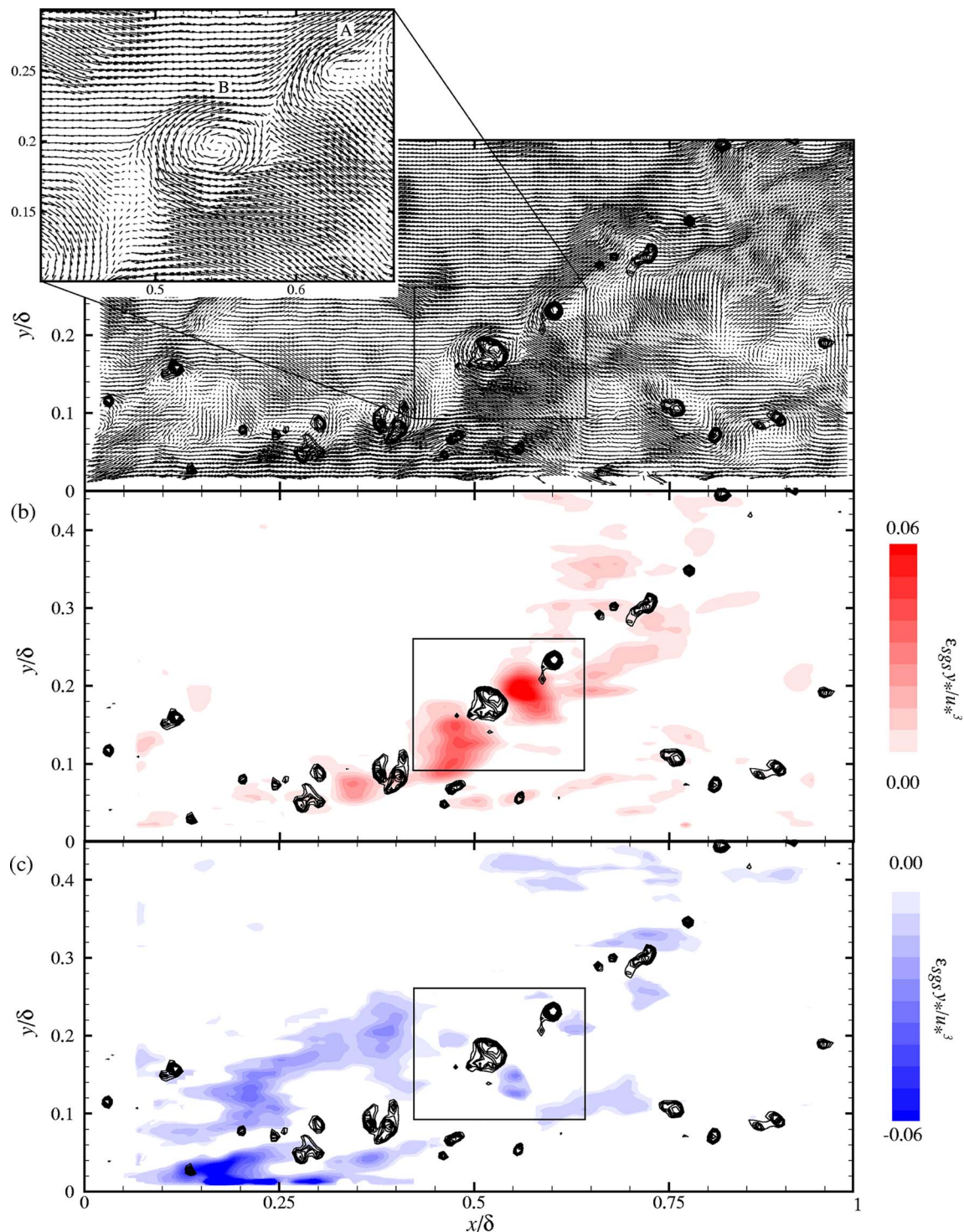


FIG. 4. (Color online) (a) Instantaneous unfiltered velocity field in the streamwise-wall-normal plane with a convection velocity $0.82U_\infty$ removed. (b) Contours of instantaneous forward scatter computed from the filtered version of the velocity field presented in (a). (c) Contours of instantaneous backscatter. Line contours of swirling strength are plotted in the background to highlight the locations of the spanwise vortex cores.

velocity gradient tensor. Swirling strength (λ_{ci}), the imaginary portion of the complex-conjugate eigenvalues of the local velocity gradient tensor, is an unambiguous identifier of rotation.^{2,3,36} Identification of vortices via λ_{ci} is superior to vorticity since it does not identify regions of strong shear that are absent of rotation and λ_{ci} yields very similar results to other $\nabla\mathbf{u}$ -based identification methods.³⁷ Both Galilean decomposition and swirling strength are used to visualize the

local kinematics induced by vortices and to efficiently identify all embedded structure, respectively.

Figure 4(a) presents a Galilean decomposition of a typical instantaneous unfiltered velocity realization in the streamwise-wall-normal plane with a constant convection velocity $0.82U_\infty$ removed (U_∞ is the free-stream velocity). Several spanwise vortex cores satisfying the aforementioned Kline and Robinson³⁵ definition are visualized in this refer-

ence frame. For comparison, contours of instantaneous swirling strength, computed from the unfiltered instantaneous velocity field, are shown in the background of the Galilean decomposition. All of the swirling motions noted in the Galilean decomposition are spatially coincident with clusters of λ_{ci} . In addition, other clusters of λ_{ci} are also noted at locations where swirling patterns are not present in the vector field because these structures are not moving at the advection velocity chosen for the Galilean decomposition.

Each of the visualized spanwise vortices in Fig. 4(a) induces a strong ejection of low-speed fluid away from the wall (a Q_2 event), sometimes generating a distinct shear layer upstream of the head due to its interaction with an accompanied inrush of higher-speed fluid from the outer region (a sweep, or Q_4 event). For brevity, the quadrant decomposition introduced by Lu and Willmarth³⁸ is used herein to describe Reynolds-stress-producing events as Q_1 ($u' > 0, v' > 0$; outward interaction), Q_2 ($u' < 0, v' > 0$; ejection), Q_3 ($u' < 0, v' < 0$; inward interaction), and Q_4 ($u' > 0, v' < 0$; sweep), where u' and v' are the fluctuating streamwise and wall-normal velocity components, respectively. The inset of Fig. 4(a) provides a zoomed-in view of two such vortices, with vortex A exhibiting a clear inclined shear layer along its back due to the interaction of opposing Q_2 and Q_4 events at $(x, y) = (0.6\delta, 0.225\delta)$, while vortex B induces an isolated ejection near $(x, y) = (0.55\delta, 0.175\delta)$. The spatial characteristics of these structures are quite consistent with the hairpin vortex signature proposed by Adrian *et al.*⁵ Therefore, these vortex cores are interpreted as slices through the spanwise-oriented heads of hairpin structures. In addition, these individual vortices appear to align in the streamwise direction with the heads of the hairpins forming an interface inclined away from the wall at an angle of 20° . A large-scale region of relatively uniform low-momentum fluid is also observed beneath the inclined interface attributable to the collective induction of the vortices. These larger-scale spatial signatures are consistent with the hairpin vortex packet observations of Adrian *et al.*⁵ It should be noted that the structural features observed in this instantaneous velocity field are apparent in nearly all of the velocity realizations acquired, indicating that such structures are a dominant feature of the outer layer.

The contributions of such structures to SGS dissipation can be clarified by computing the instantaneous forward- and backward-scatter fields associated with the instantaneous velocity realization presented in Fig. 4(a). Figure 4(b) presents contours of forward scatter overlaid upon line contours of swirling strength to accentuate the positions of the hairpin heads relative to strong energy transfer events. Clusters of significant forward scatter are found to exist between consecutive hairpin heads in the visualized packet. Examination of the instantaneous velocity field around the individual hairpin heads [as shown in the inset to Fig. 4(a)] and the associated forward scatter in Fig. 4(b) reveals that regions of forward scatter are spatially coincident with strong ejections of low-speed fluid away from the wall, just upstream and below the head of each vortex. In particular, the strongest forward-scatter event in this instantaneous field occurs just below and upstream of vortex A in the region where opposing Q_2 and Q_4 events meet to form an inclined shear layer.

While vortex B still generates a significant forward-scatter event just below/upstream of its head, it is noticeably weaker than that associated with vortex A, likely because its ejection event is not accompanied by a discernible sweep event. Therefore, this instantaneous example illustrates that shear layers formed by the interaction of ejection-sweep events between adjacent vortices, in conjunction with the collectively induced ejections of low-speed fluid by the vortices in a hairpin packet, generate a relatively large-scale forward-scatter interface that is spatially coincident with the inclined interface formed by the heads of the hairpins. This large-scale region of instantaneous forward scatter represents a significant transfer of energy from large to small scales.

In contrast, weak, localized instantaneous backscatter events are concentrated around the hairpin heads [Fig. 4(c)]. These backscatter events appear just upstream/above and downstream/below each hairpin head in the packet, with the latter consistently more intense than the former. In addition, a larger-scale and more intense instantaneous backscatter event is noted at the trailing edge of the packet near $(x, y) = (0.2\delta, 0.1\delta)$. All of these instantaneous clusters of backscatter represent energy transfer from the smaller to the larger scales and some of these events are just as intense as the forward-scatter events observed in Fig. 4(b). Further, it is remarkable that nearly all of the significant instantaneous energy-transfer events, both forward and backward scatter, are concentrated around the embedded vortical structures with little activity elsewhere in the instantaneous field. This behavior indicates that such structures play an important, if not dominant, role in interscale energy transfer. Finally, the clustering of forward- and backward-scatter events around vortical structures is notable in the vast majority of the instantaneous fields.

As detailed in Eq. (7), the instantaneous forward-scatter and backscatter fields presented in Fig. 4 embody contributions from three SGS stress-filtered strain-rate products: $-\tau_{11}\tilde{S}_{11}$, $-\tau_{12}\tilde{S}_{12}$, and $-\tau_{22}\tilde{S}_{22}$. These contributions to the forward- and backward-scatter fields of Fig. 4 are computed and presented as Fig. 5, revealing that the intense, instantaneous forward scatter observed upstream and below each vortex core is attributable to a combination of $-\tau_{11}\tilde{S}_{11}$ and $-\tau_{12}\tilde{S}_{12}$. Of particular interest are the contributions to the forward-scatter events observed upstream and below of vortices A and B in Fig. 4. As noted earlier, the forward-scatter event associated with vortex A (which is spatially coincident with opposing Q_2 and Q_4 events) is much stronger than the forward-scatter event associated with vortex B (which is spatially coincident with an isolated Q_2 event). Figure 5 indicates that while the $-\tau_{12}\tilde{S}_{12}$ contributions to each of these forward-scatter events are comparable in magnitude, the $-\tau_{11}\tilde{S}_{11}$ contribution is much larger in the case of vortex A. Therefore, while strong ejection (Q_2) events generate forward scatter through $-\tau_{12}\tilde{S}_{12}$ for vortices A and B, the opposing Q_2 and Q_4 events upstream and below of vortex A generate a significant \tilde{S}_{11} event that then contributes additionally to forward scatter through $-\tau_{11}\tilde{S}_{11}$. In contrast, the strong backscatter noted upstream/above and downstream/below

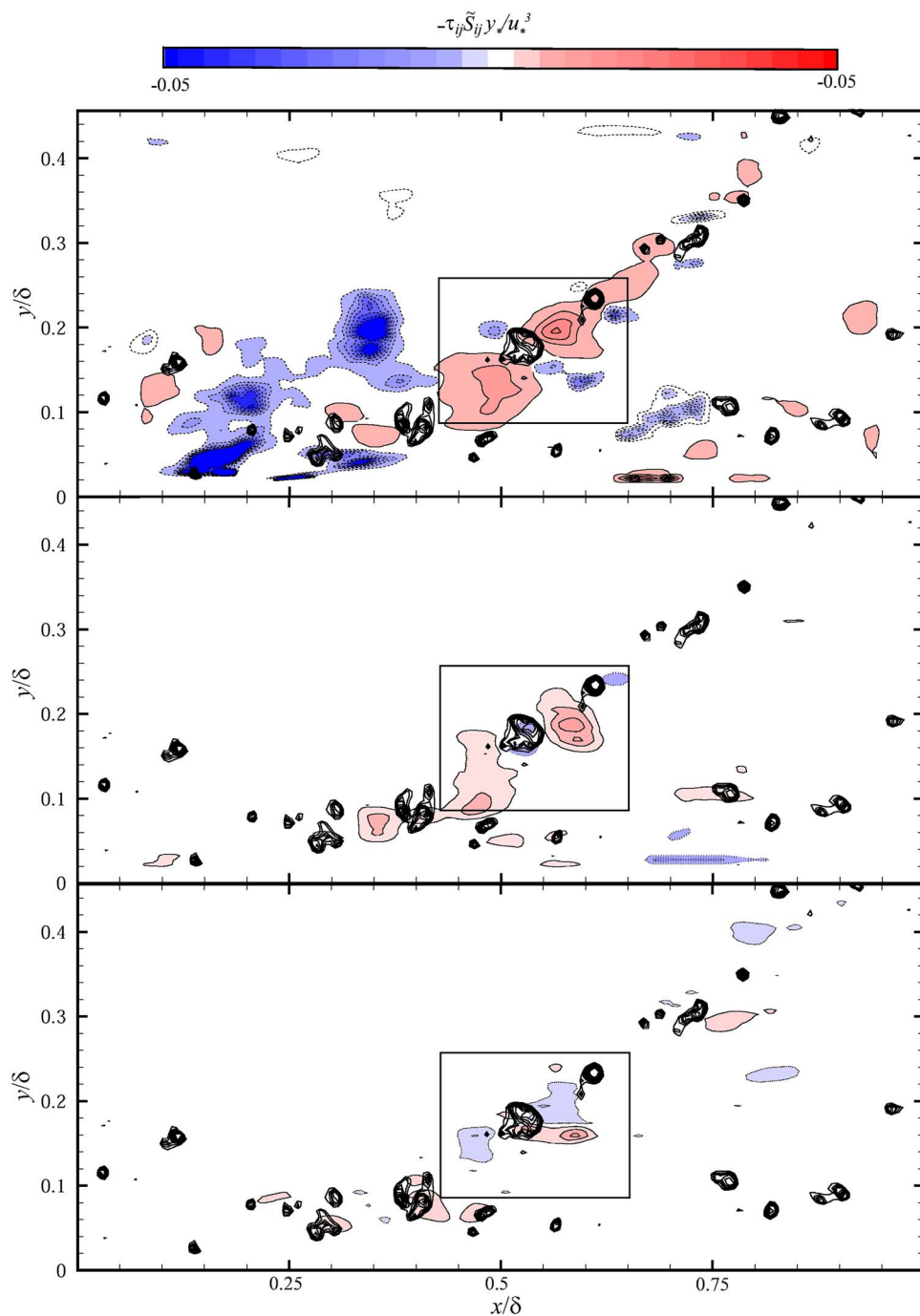


FIG. 5. (Color online) Contributions of instantaneous (a) $-\tau_{11}\tilde{S}_{11}$, (b) $-\tau_{12}\tilde{S}_{12}$, and (c) $-\tau_{22}\tilde{S}_{22}$ to the instantaneous forward and backward scatter fields presented in Fig. 4. Dashed contour lines represent negative values.

each spanwise vortex, as well as the intense backscatter event at the tail of the vortex packet, is attributable entirely to $-\tau_{11}\tilde{S}_{11}$. Interestingly, $-\tau_{22}\tilde{S}_{22}$ is found to contribute very little to the dominant, instantaneous subgrid-scale energy transfer events noted in Fig. 4.

V. STATISTICAL ANALYSIS

Given the remarkable spatial coincidence of significant forward- and backward-scatte events with individual hairpin vortices and their larger-scale organization into packets, statistical experiments are performed using spatial correlations and conditional averaging techniques to confirm that this behavior occurs consistently in the presence of such structures.

Of primary interest is determining the average forward- and backward-scatte patterns induced by individual hairpin vortices and hairpin vortex packets. The best estimate of this average field is the conditional average of the forward or backward scatte field given the presence of a spanwise vortex core (represented by λ_{ci}): $\langle \Phi(\mathbf{x}') | \lambda_{ci}(\mathbf{x}) \rangle$. While direct assessment of this conditional average is difficult because of the enormous number of events that must be included for statistical convergence, it instead can be estimated using stochastic estimation.³⁹ Stochastic estimation is a powerful technique for estimating conditional averages from unconditional correlation data.⁴⁰ An estimate is achieved by minimizing the mean-square error between the true conditional

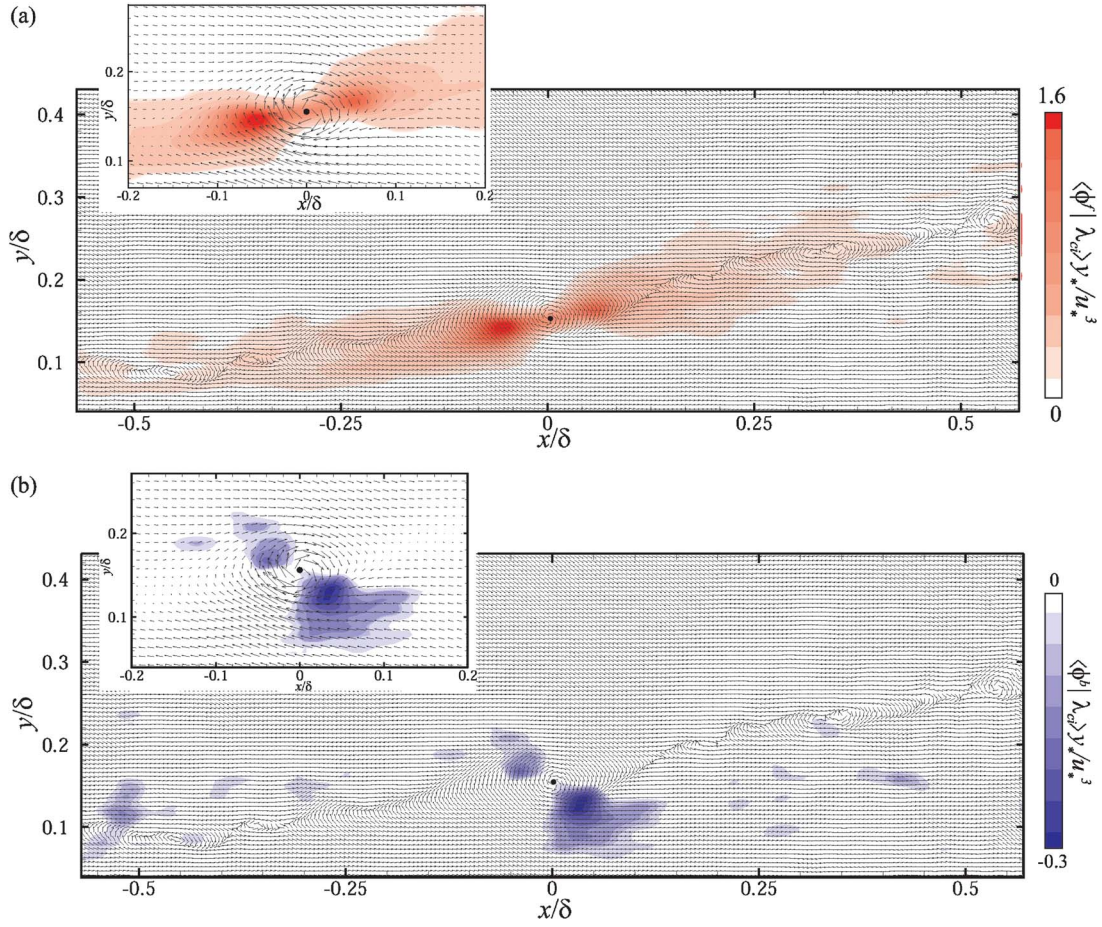


FIG. 6. (Color online) Contours of (a) $\langle \phi^f | \lambda_{ci} \rangle$ and (b) $\langle \phi^b | \lambda_{ci} \rangle$ at $y_{\text{ref}} = 0.15\delta$. The stochastic estimate of $\langle u'_j | \lambda_{ci} \rangle$ at $y_{\text{ref}} = 0.15\delta$, with all vectors normalized to unity by their respective magnitudes, is overlaid for comparison and the event location is indicated by a solid circle. Every other vector is removed for clarity and the vectors in the insets are shown in un-normalized form.

average and a given estimate, with linear estimates yielding excellent approximations of true conditional averages^{7,41} (a comprehensive review of linear stochastic estimation and its application to turbulence is given by Adrian⁴²). Therefore, the conditional average postulated above can be estimated in a linear fashion as

$$\langle \Phi(\mathbf{x}') | \lambda_{ci}(\mathbf{x}) \rangle \approx L \lambda_{ci}(\mathbf{x}), \quad (9)$$

where the kernel L is determined by minimizing the mean-square error between the estimate and the conditional average, yielding

$$\langle \Phi(\mathbf{x}') | \lambda_{ci}(\mathbf{x}) \rangle \approx \frac{\langle \lambda_{ci}(\mathbf{x}) \Phi(\mathbf{x}') \rangle}{\langle \lambda_{ci}(\mathbf{x}) \lambda_{ci}(\mathbf{x}) \rangle} \lambda_{ci}(\mathbf{x}). \quad (10)$$

Therefore, the average forward- or backward-scatter field (represented by Φ) associated with a hairpin vortex can be estimated via the unconditional two-point correlations

$$R_{\lambda\Phi}(r_x, y) = \langle \lambda_{ci}(x, y_{\text{ref}}) \Phi(x + r_x, y) \rangle, \quad (11)$$

where r_x represents the spatial separation in the streamwise direction.

Stochastic estimation is often used to study the dominant features of canonical turbulent flows and several examples are presented in Adrian.⁴² Most recently, Christensen and Adrian⁷ used linear stochastic estimation to uncover the av-

erage velocity field associated with a spanwise vortex core (the head of a hairpin) in turbulent channel flow. This estimate took the form

$$\langle u'_j(\mathbf{x}') | \lambda_{ci}(\mathbf{x}) \rangle \approx \frac{\langle \lambda_{ci}(\mathbf{x}) u'_j(\mathbf{x}') \rangle}{\langle \lambda_{ci}(\mathbf{x}) \lambda_{ci}(\mathbf{x}) \rangle} \lambda_{ci}(\mathbf{x}), \quad (12)$$

where u'_j is the j th fluctuating velocity component. This estimate revealed not only a swirling pattern consistent with the spanwise vortices noted in the instantaneous example presented in Fig. 4 but also uncovered a well-defined set of streamwise-aligned swirling motions inclined away from the wall at a shallow angle. This pattern was interpreted to be the statistical imprint of large-scale hairpin vortex packets. This estimate of the conditionally averaged unfiltered velocity field associated with a spanwise vortex core is repeated here to aid in interpreting the estimates of the conditionally averaged forward- and backward-scatter fields.

The estimate of the conditionally averaged forward-scatter field associated with a spanwise vortex core, $\langle \phi^f | \lambda_{ci} \rangle$, is presented in Fig. 6(a) for $y_{\text{ref}} = 0.15\delta$. Superimposed on the contours of $\langle \phi^f | \lambda_{ci} \rangle$ is the estimate of the conditionally averaged velocity field associated with a spanwise vortex core, $\langle u'_j | \lambda_{ci} \rangle$, given by Eq. (12). As noted by Christensen and Adrian,⁷ this stochastically estimated velocity field is stron-

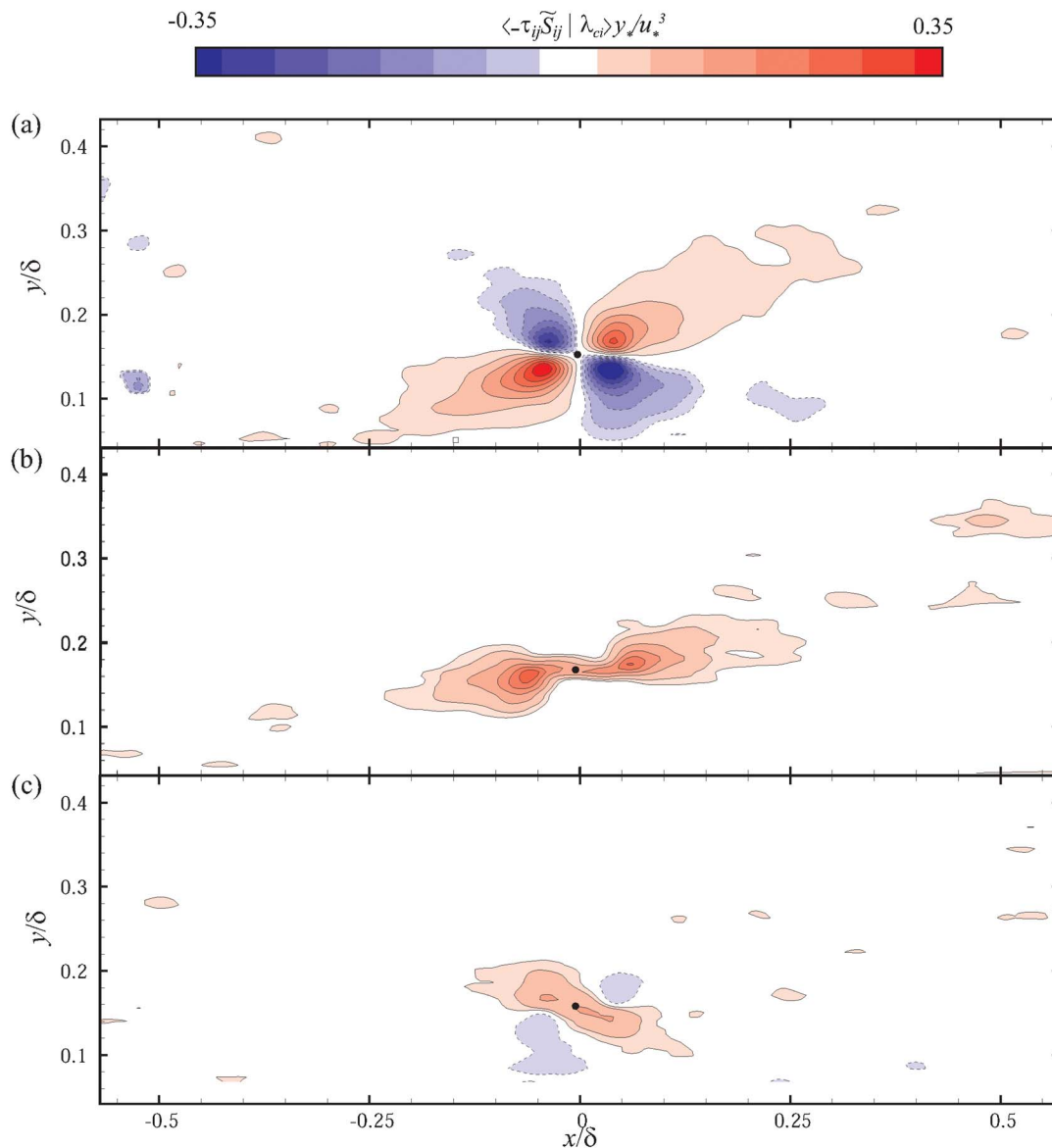


FIG. 7. (Color online) Contours of (a) $\langle -\tau_{11}\tilde{S}_{11} | \lambda_{ci} \rangle$, (b) $\langle -\tau_{12}\tilde{S}_{12} | \lambda_{ci} \rangle$, and (c) $\langle -\tau_{22}\tilde{S}_{22} | \lambda_{ci} \rangle$ at $y_{\text{ref}}=0.15\delta$. Dashed contour lines represent negative values and the event location is indicated by a solid circle.

gest around the event location since this is where the spatial correlations forming the basis of the estimate are largest. Consequently, the weaker vectors located away from the event location tend to be overwhelmed by the larger vectors surrounding the event location. Hence, following Christensen and Adrian,⁷ all vectors in Fig. 6(a) are normalized by their respective magnitudes, yielding a direction field. This vector field clearly illustrates the presence of a distinct inclined interface representative of the statistical imprint of hairpin vortex packets. A large-scale region of considerable forward scatter is found to exist along the entire inclined interface of the vortex packet, indicating that this inclined interface, which forms the “backbone” of a vortex packet, generates significant SGS energy transfer from the large to small scales. The inset of Fig. 6(a) contains a zoomed-in view of the forward-scatter field around the event location along with the overlaid estimate of $\langle u'_j | \lambda_{ci} \rangle$ in unnormalized form and reveals two particularly intense peaks

just below/upstream and above/downstream of the spanwise vortex event location, with the latter stronger than the former. Both the large-scale region of forward scatter as well as the intense forward-scatter peaks localized around the spanwise vortex are quite consistent with the instantaneous forward-scatter events and the associated velocity field presented in Fig. 4.

The estimate of the conditionally averaged backscatter field associated with a spanwise vortex core, $\langle \phi^b | \lambda_{ci} \rangle$, is presented in Fig. 6(b) along with $\langle u'_j | \lambda_{ci} \rangle$. Localized peaks in backscatter are noted just above/upstream and below/downstream of the vortex core, with the latter larger in magnitude and extent. This observation is consistent with the instantaneous backscatter behavior noted in Fig. 4. Beyond the backscatter observed in the immediate vicinity of the vortex event, a relatively strong region of backscatter is also noted near $(x, y) = (-0.5\delta, 0.1\delta)$, coincident with the trailing

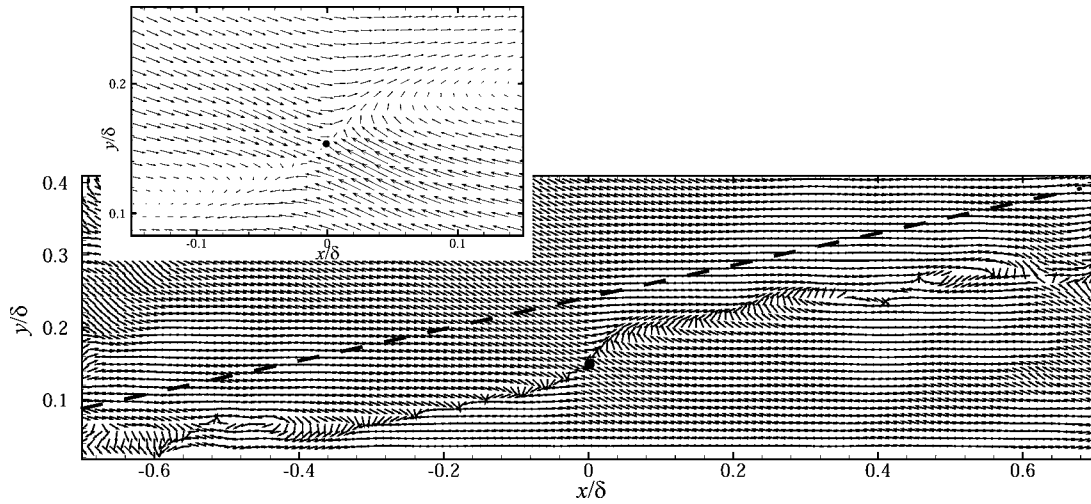


FIG. 8. Linear stochastic estimate of $\langle u'_j | \phi^f \rangle$ at $y_{\text{ref}} = 0.15\delta$. The event location is indicated by a solid circle and all vectors are normalized to unity by their respective magnitudes. The inset shows a magnified view of the un-normalized velocity field around the event location. Every other vector is removed for clarity in both cases and the dashed line highlights the inclination angle of the observed structure.

end of the average vortex packet structure apparent in $\langle u'_j | \lambda_{ci} \rangle$. This backscatter is quite similar to the region of instantaneous backscatter noted at the tail end of the instantaneous hairpin packet in Fig. 4(c), indicating that it is a consistent feature of most hairpin packets since it has survived the averaging process required to estimate $\langle \phi^f | \lambda_{ci} \rangle$.

As observed in Sec. IV, dominant forward-scatter and backscatter events can be attributed to significant $-\tau_{11}\tilde{S}_{11}$, $-\tau_{12}\tilde{S}_{12}$, and/or $-\tau_{22}\tilde{S}_{22}$ events. Therefore, the average contributions of each of these terms to the forward- and backward-scatter fields in Fig. 6 are computed. Figure 7(a) presents $\langle -\tau_{11}\tilde{S}_{11} | \lambda_{ci} \rangle$ at $y_{\text{ref}} = 0.15\delta$ and reveals that $-\tau_{11}\tilde{S}_{11}$ is a dominant contributor to the forward scatter induced by individual hairpin vortices and their larger-scale organization into packets, including the forward-scatter peaks noted below/upstream and above/downstream of the event location. In addition, $-\tau_{11}\tilde{S}_{11}$ generates significant backscatter both upstream/above and downstream/below of the event location and accounts for the backscatter patterns noted in Fig. 6(b) around the event location. A strong backward-scatter peak is also notable in $\langle -\tau_{11}\tilde{S}_{11} | \lambda_{ci} \rangle$ near $x = -0.5\delta$, which is spatially coincident with the backscatter observed at the trailing end of the average packet structure in Fig. 6(b). These observations are entirely consistent with the contributions of $-\tau_{11}\tilde{S}_{11}$ to instantaneous forward and backward scatter [Fig. 5(a)]. Figure 7(b) presents $\langle -\tau_{12}\tilde{S}_{12} | \lambda_{ci} \rangle$ and reveals that $-\tau_{12}\tilde{S}_{12}$ contributes nearly equally with $-\tau_{11}\tilde{S}_{11}$ to the large-scale forward-scatter interface and the strong forward-scatter peaks noted in Fig. 6(a), consistent with the instantaneous evidence presented in Fig. 5(b). Finally, $-\tau_{22}\tilde{S}_{22}$ [Fig. 7(c)] is found to generate weak backscatter spatially coincident to the strong forward-scatter contributions of both $-\tau_{11}\tilde{S}_{11}$ and $-\tau_{12}\tilde{S}_{12}$. In addition, $-\tau_{22}\tilde{S}_{22}$ generates localized regions of weak forward scatter overlapping the regions of backscatter generated by $-\tau_{11}\tilde{S}_{11}$. It should be noted that $-\tau_{11}\tilde{S}_{11}$ appears to be solely responsible for the backscatter observed at the

upstream tail of hairpin packets as neither $-\tau_{12}\tilde{S}_{12}$ nor $-\tau_{22}\tilde{S}_{22}$ show any appreciable backscatter in this region.

While the results presented in Figs. 6 and 7 indicate that individual hairpin vortices and larger-scale hairpin packets generate significant transfer of energy to and from the small scales, it is not known whether these features represent the most dominant kinematic events associated with interscale energy transfer. Therefore, rather than conditioning on the presence of a spanwise vortex, the average unfiltered fluctuating velocity fields associated with significant forward- and backward-scatter events are statistically reconstructed by linear stochastic estimation to reveal the most probable kinematic patterns associated with such events. Figure 8 presents the estimate of the fluctuating velocity field given the presence of a forward-scatter event, $\langle u'_j | \phi^f \rangle$, at $y_{\text{ref}} = 0.15\delta$. (As was done in Fig. 6, all vectors in this figure are normalized by their magnitudes, yielding a direction field.) The forward-scatter event (represented by the solid circle) is accompanied by the formation of a shear layer between opposing Q_2 and Q_4 events. This behavior is clearly evident in the inset to Fig. 8, which shows a magnified view of the fluctuating velocity field in the immediate vicinity of the event location. The lengths of the vectors depicted in this inset are representative of their true magnitudes and they clearly show a strong Q_2 event occurring beneath the forward-scatter event location with a Q_4 event just above the event, resulting in the formation of an inclined shear layer. This observation is consistent with the behavior noted in Figs. 4 and 5 for instantaneous vortex A where the strongest instantaneous forward-scatter event occurs at the interface of opposing Q_2 and Q_4 events. This forward scatter is generated jointly by $-\tau_{12}\tilde{S}_{12}$ via the strong ejection event and $-\tau_{11}\tilde{S}_{11}$ due to intense \tilde{S}_{11} at the opposing Q_2 - Q_4 interface. This behavior is also consistent with the results of Carper and Porte-Agel,²⁷ which showed that a strong forward-scatter event was locally accompanied by a converging flow pattern in the conditionally averaged velocity field. Of particular significance, and a behavior not

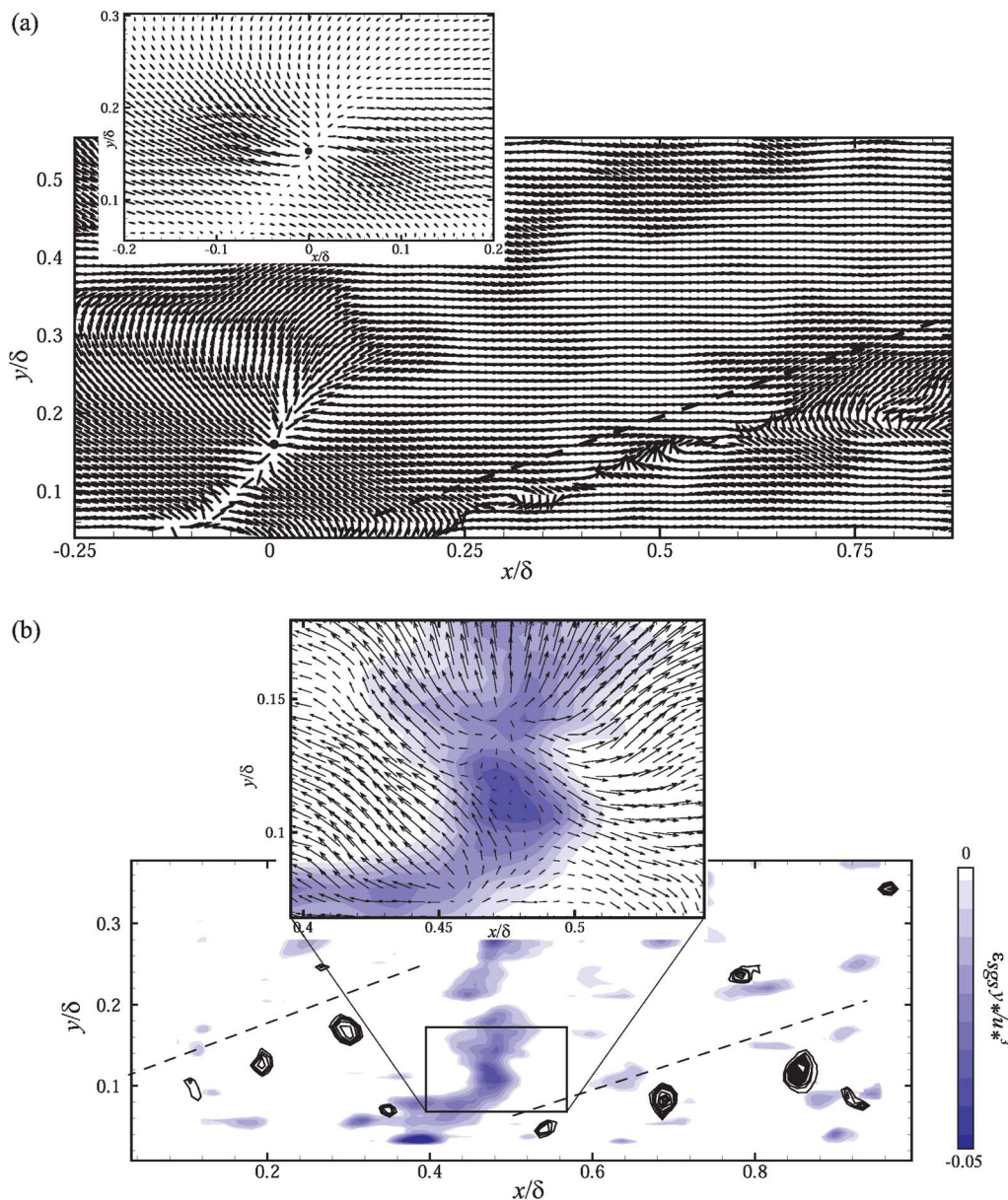


FIG. 9. (Color online) (a) Linear stochastic estimate of $\langle u'_j | \phi^b \rangle$ at $y_{\text{ref}} = 0.15\delta$. The event location is indicated by a solid circle and all vectors are normalized to unity by their respective magnitudes. The inset shows a magnified view of the un-normalized velocity field around the event location. Every other vector is removed for clarity in both cases. (b) Instantaneous backscatter field, with line contours of λ_{ci} in the background, illustrating the presence of significant backscatter at the trailing edge of a vortex packet. The inset illustrates the local velocity pattern around the backscatter event. The dashed lines highlight the inclination angles of the observed structures.

noted in the literature, is the fact that this localized shear-layer structure is part of a much larger-scale shear-layer pattern spanning a length of 1.5δ in the streamwise direction and inclined slightly away from the wall. In addition, a distinct zone of low-speed fluid is observed under the inclined interface. These spatial characteristics are consistent with estimates of the conditionally averaged packet structure observed by Christensen and Adrian⁷ and presented in Fig. 6, along with the instantaneous packet example noted in Fig. 4. This observation, along with the large-scale region of forward scatter noted in $\langle \phi^f | \lambda_{ci} \rangle$ [Fig. 6(a)], indicates that, on average, significant transfer of energy from the large to the small scales occurs along the “backbone” of hairpin vortex

packets due to the collectively induced ejections and sweeps associated with these structures.

Figure 9(a) presents the estimate of the conditionally averaged unfiltered fluctuating velocity field given a backscatter event, $\langle u'_j | \phi^b \rangle$, at $y_{\text{ref}} = 0.15\delta$. This average velocity field illustrates that the most probable velocity field associated with energy transfer from the small to the large scales is a diverging pair of Q_2 and Q_4 events upstream/above and downstream/below of the event location, respectively (the vector magnitudes are set to unity, yielding a direction field). This behavior is clearly observed in the inset of Fig. 9(a), which shows a magnified view of the un-normalized velocity field around the backscatter event. This diverging pattern lo-

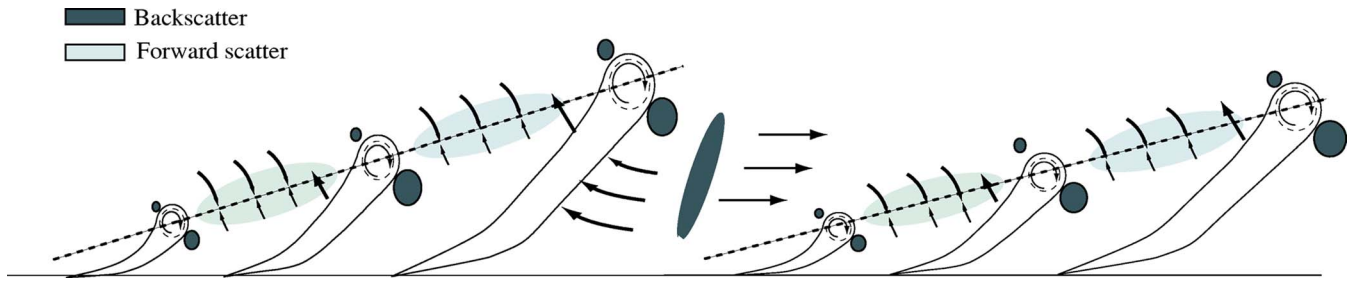


FIG. 10. (Color online) Conceptual model illustrating the role of hairpin vortices and their organization into larger-scale packets in the transfer of energy within the log layer of wall turbulence.

cal to the backscatter event is consistent with the conditionally averaged field obtained by Carper and Porte-Agel.²⁷ However, of greater significance is the existence of a large-scale inclined shear-layer structure downstream of the backscatter event location, consistent with the statistical imprint of a hairpin vortex packet, $\langle u'_j | \lambda_{ci} \rangle$, presented in Fig. 6. These characteristics are quite similar to the relatively intense region of instantaneous backscatter noted at the trailing edge of the instantaneous vortex packet presented in Fig. 4(c) and the behavior noted in the estimates of $\langle \phi^b | \lambda_{ci} \rangle$ [Fig. 6(b)] and $\langle -\tau_{11} \tilde{S}_{11} | \lambda_{ci} \rangle$ [Fig. 7(a)]. An additional instantaneous example of such behavior is presented in Fig. 9(b) in which two hairpin vortex packets are identified via line contours of λ_{ci} overlaid upon contours of instantaneous backscatter. Intense backscatter is observed between these consecutive vortex packets, closer in proximity to the trailing end of the downstream vortex packet than the leading end of the upstream packet. The occurrence of this intense backscatter at the tail of the downstream packet in Fig. 9(b) is quite consistent with the stochastically estimated velocity field $\langle u'_j | \phi^b \rangle$ of Fig. 9(a). The inset of Fig. 9(b) presents a zoomed-in view of the instantaneous velocity field in the reference frame of the downstream vortex packet and a clear diverging pair of Q_2 and Q_4 events is noted, strikingly similar to the local average velocity field $\langle u'_j | \phi^b \rangle$ shown in the inset of Fig. 9(a). Therefore, while localized backscatter is consistently noted upstream/above and downstream/below of spanwise vortex cores, these vortices are not the most probable kinematic contributors to backscatter. Rather, the trailing edges of hairpin packets appear to represent the most likely contributors to intense backscatter. If one were to consider the possibility that vortex packets propagate coherently one behind the other, as postulated recently by Kim and Adrian⁶ and as observed in Fig. 9(b), the interaction of the induced low-momentum region beneath the upstream packet with the induced high-momentum fluid above the downstream packet would generate a diverging pair of Q_2 and Q_4 events similar to the patterns noted in the insets of Figs. 9(a) and 9(b).

VI. SUMMARY AND CONCLUSIONS

The results presented herein suggest that hairpin vortices and their larger-scale organization into vortex packets contribute significantly to interscale energy transfer in the log layer. Instantaneous forward scatter is observed between con-

secutive hairpin heads within a packet near the intense Q_2 events induced by the individual vortices attributable to $-\tau_{12} \tilde{S}_{12}$ contributions to ε_{sgs} . Often the most intense instantaneous forward-scanter events are noted when these ejections are opposed by sweep (Q_4) events, forming inclined shear layers along the backs of the hairpins. In these situations, forward scatter is due not only to $-\tau_{12} \tilde{S}_{12}$ contributions but also strong contributions from $-\tau_{11} \tilde{S}_{11}$, likely associated with significant \tilde{S}_{11} across the Q_2 - Q_4 interface. In contrast, localized backscatter is noted upstream/above and downstream/below each hairpin head, with the latter consistently stronger than the former. Finally, a region of significant instantaneous backscatter is often noted at the trailing edge of a vortex packet, particularly when a second packet is observed at its upstream end.

These instantaneous observations are corroborated by estimates of the conditionally averaged forward and backward scatter fields given the presence of a spanwise vortex core (a hairpin head). Significant forward scatter is found to occur, on average, along the inclined interface formed by the heads of the hairpins in a vortex packet, with the strongest forward-scanter contributions coming from the $-\tau_{12} \tilde{S}_{12}$ and $-\tau_{11} \tilde{S}_{11}$ terms. In contrast, localized backscatter around the hairpin heads is noted in estimates of the conditionally averaged backscatter field given the presence of a vortex core, principally due to $-\tau_{11} \tilde{S}_{11}$ contributions to ε_{sgs} . This estimate also reveals a strong region of backscatter far upstream ($\sim 0.5\delta$) of the event location attributable to $-\tau_{11} \tilde{S}_{11}$, coincident with the trailing edge of the average packet structure represented by $\langle u'_j | \lambda_{ci} \rangle$ and consistent with the significant backscatter noted at the trailing edge of instantaneous vortex packets. This latter observation indicates that most packets generate a significant backscatter event at their trailing edge since this phenomenon survives the averaging process used to estimate $\langle \phi^b | \lambda_{ci} \rangle$.

In order to determine the most probable kinematic events associated with forward- and backward-scanter events, the average velocity fields associated with forward and backward scatter are reconstructed using linear stochastic estimation. The estimate of the conditionally averaged velocity field given a forward-scanter event reveals a localized shear layer generated by opposing Q_2 and Q_4 events around the forward-scanter event. This localized shear layer is found to be part of a much larger-scale inclined interface, consistent

with the statistical imprint of hairpin vortex packets observed by Christensen and Adrian⁷ and presented herein. This observation, in conjunction with the instantaneous fields and the conditionally averaged forward-scatter field given a vortex core, illustrates that, although the ejections produced by the hairpins in a vortex packet generate large-scale regions of forward scatter, the most intense forward-scatter events occur in the presence of opposing Q_2 and Q_4 events. In contrast, the estimate of the conditionally averaged velocity field associated with a backscatter event reveals a diverging flow pattern that forms at the trailing end of an inclined shear layer, the latter of which is again consistent with the statistical imprint of hairpin vortex packets. Therefore, while the individual hairpin heads generate weak backscatter locally, the most probable kinematic event associated with backscatter is in fact a diverging pair of Q_2 and Q_4 events at the trailing end of a vortex packet. Such patterns are observed in instantaneous fields, particularly between two consecutive vortex packets aligned in the streamwise direction. In addition, the fact that these imprints of vortex organization have survived the unconditional averaging process of stochastic estimation speaks to the robust and dominant role that such structures play in the physics of wall turbulence. Further, while the forward- and backward-scatter events locally generated by the individual hairpin vortices reported here are consistent with the recent atmospheric observations of Carper and Porte-Agel,²⁷ indicating that measurements of canonical wall-bounded flows at moderate Re may be suitable for modeling high-Re behavior, the evidence presented herein regarding the role of hairpin vortex packets in SGS energy transfer represent new and fundamentally important observations in the area of SGS modeling.

Finally, a composite conceptual scenario that accounts for all of the energy-transfer behavior observed is presented in Fig. 10. While individual hairpin vortices generate significant localized forward scatter of energy, their coherent alignment into larger-scale entities yields collectively induced, large-scale regions of intense forward scatter coincident with the inclined interface of the vortex packets. In contrast, while individual vortices generate somewhat weak localized backscatter, the possible coherent alignment of hairpin vortex packets in the streamwise direction, as proposed by Kim and Adrian,⁶ may account for the generation of significant backscatter between the trailing edge of one packet and the leading edge of another. In particular, this backward scatter of energy may represent a net energy transfer from the smallest hairpin in the downstream packet to the largest hairpin of the upstream packet. Unfortunately, the present data is limited to instantaneous planar slices of the flow over a relatively limited streamwise field of view. As such, the proposed structural model of interscale energy transfer represents only one possible scenario to explain the observations presented herein. Analysis of instantaneous 3D fields from DNS, for example, would further clarify the suitability of this conceptual model. Nevertheless, the present results link dominant SGS energy transfer to and from the small scales to large-scale structures consistent with hairpin vortex packets.

ACKNOWLEDGMENTS

The boundary-layer measurements were performed by Y. Wu and supported by the Air Force Office of Scientific Research under Grant No. FA9550-05-1-0043 (Dr. Rhett Jeffries, Program Manager). The analysis portion of this effort was supported by the University of Illinois. We are indebted to Professor Robert Moser and Professor Javier Jimenez (and co-workers) for making their $Re_\tau=940$ channel-flow DNS data available.

- ¹C. R. Smith, "A synthesized model of the near-wall behavior in turbulent boundary layers," in *Proceedings of the 8th Symposium on Turbulence*, University of Missouri-Rolla, Rolla, MI, 1984, pp. 299–325.
- ²J. Zhou, R. J. Adrian, and S. Balachandar, "Autogeneration of near-wall vortical structures in channel flow," *Phys. Fluids* **8**, 288 (1996).
- ³J. Zhou, R. J. Adrian, S. Balachandar, and T. M. Kendall, "Mechanisms for generating coherent packets of hairpin vortices in channel flow," *J. Fluid Mech.* **387**, 353 (1999).
- ⁴M. R. Head and P. Bandyopadhyay, "New aspects of turbulent boundary-layer structure," *J. Fluid Mech.* **107**, 297 (1981).
- ⁵R. J. Adrian, C. D. Meinhart, and C. D. Tomkins, "Vortex organization in the outer region of the turbulent boundary layer," *J. Fluid Mech.* **422**, 1 (2000).
- ⁶K. C. Kim and R. J. Adrian, "Very large-scale motion in the outer layer," *Phys. Fluids* **11**, 417 (1999).
- ⁷K. T. Christensen and R. J. Adrian, "Statistical evidence of hairpin vortex packets in wall turbulence," *J. Fluid Mech.* **431**, 433 (2001).
- ⁸I. Marusic, "On the role of large-scale structures in wall turbulence," *Phys. Fluids* **13**, 735 (2001).
- ⁹Z.-C. Liu, R. J. Adrian, and T. J. Haratty, "Large-scale modes of turbulent channel flow: Transport and structure," *J. Fluid Mech.* **448**, 53 (2001).
- ¹⁰B. Ganapathisubramani, E. K. Longmire, and I. Marusic, "Characteristics of vortex packets in turbulent boundary layers," *J. Fluid Mech.* **478**, 35 (2003).
- ¹¹R. Rogallo and P. Moin, "Numerical simulation of turbulent flows," *Annu. Rev. Fluid Mech.* **15**, 99 (1984).
- ¹²C. Meneveau and J. Katz, "Scale-invariance and turbulent models for large-eddy simulation," *Annu. Rev. Fluid Mech.* **32**, 1 (2000).
- ¹³U. Piomelli and E. Balaras, "Wall-layer models for large-eddy simulations," *Annu. Rev. Fluid Mech.* **34**, 349 (2002).
- ¹⁴U. Piomelli, W. H. Cabot, P. Moin, and S. Lee, "Subgrid-scale backscatter in turbulent and transitional flows," *Phys. Fluids A* **3**, 1766 (1991).
- ¹⁵C. Meneveau, "Statistics of turbulence subgrid-scale stresses: Necessary conditions and experimental tests," *Phys. Fluids* **6**, 815 (1994).
- ¹⁶R. A. Clark, J. H. Ferziger, and W. C. Reynolds, "Evaluation of subgrid-scale models using an accurately simulated turbulent flow," *J. Fluid Mech.* **91**, 1 (1979).
- ¹⁷J. A. Domaradzki, W. Liu, and M. E. Brachet, "An analysis of subgrid-scale interactions in numerically simulated isotropic turbulence," *Phys. Fluids A* **5**, 1747 (1993).
- ¹⁸C. Hartel and L. Kleiser, "Analysis and modelling of subgrid-scale motions in near-wall turbulence," *J. Fluid Mech.* **356**, 327 (1998).
- ¹⁹S. Liu, C. Meneveau, and J. Katz, "On the properties of similarity subgrid-scale models as deduced from measurements in a turbulent jet," *J. Fluid Mech.* **275**, 83 (1994).
- ²⁰S. Cerutti and C. Meneveau, "Statistics of filtered velocity in grid and wake turbulence," *Phys. Fluids* **12**, 1143 (2000).
- ²¹J. O'Neil and C. Meneveau, "Subgrid-scale stresses and their modelling in a turbulent plane wake," *J. Fluid Mech.* **349**, 253 (1997).
- ²²K. A. Buch and W. J. A. Dahm, "Experimental study of the fine-scale structure of conserved scalar mixing in turbulent shear flow. Part 2. $Sc \approx 1$," *J. Fluid Mech.* **364**, 1 (1998).
- ²³C. L. Lin, "Near-grid-scale energy transfer and coherent structures in the convective planetary boundary layer," *Phys. Fluids* **11**, 3482 (1999).
- ²⁴H. S. Kang and C. Meneveau, "Effect of large-scale coherent structures on subgrid-scale stress and strain-rate eigenvector alignments in turbulent shear flow," *Phys. Fluids* **17**, 055103 (2005).
- ²⁵C. Hartel, L. Kleiser, F. Unger, and R. Friedrich, "Subgrid-scale energy transfer in the near-wall region of turbulent flows," *Phys. Fluids* **6**, 3130 (1994).
- ²⁶U. Piomelli, Y. Yu, and R. J. Adrian, "Subgrid-scale energy transfer and

- near-wall turbulence structure,” *Phys. Fluids* **8**, 215 (1996).
- ²⁷M. A. Carper and F. Porte-Agel, “The role of coherent structures in subfilter-scale dissipation of turbulence measured in the atmospheric surface layer,” *J. Turbul.* **5**, 1 (2004).
- ²⁸Y. Wu and K. T. Christensen, “Population trends of spanwise vortices in wall turbulence,” *J. Fluid Mech.* (to be published).
- ²⁹C. D. Meinhart, “Investigation of turbulent boundary-layer structure using particle-image velocimetry,” Ph.D. thesis, Department of Theoretical and Applied Mechanics, University of Illinois at Urbana-Champaign, Urbana, IL, 1994.
- ³⁰J. Carlier and M. Stasnislas, “Experimental study of eddy structures in a turbulent boundary layer using particle image velocimetry,” *J. Fluid Mech.* **535**, 143 (2005).
- ³¹S. Völker, R. D. Moser, and P. Venugopal, “Optimal large eddy simulation of turbulent channel flow based on direct numerical simulation statistical data,” *Phys. Fluids* **14**, 3675 (2002).
- ³²F. Porte-Agel, M. B. Parlange, C. Meneveau, W. E. Eichinger, and M. Pahlow, “Subgrid-scale dissipation in the atmospheric surface layer: Effects of stability and filter dimension,” *J. Hydrometeor.* **1**, 75 (2000).
- ³³C. Tong, J. C. Wyngaard, S. Khanna, and J. G. Brasseur, “Resolvable- and subgrid-scale measurement in the atmospheric surface layer: Technique and issues,” *J. Atmos. Sci.* **55**, 3114 (1998).
- ³⁴J. C. Del Alamo, J. Jimenez, P. Zandonade, and R. D. Moser, “Scaling of the energy spectra of turbulent channels,” *J. Fluid Mech.* **500**, 135 (2004).
- ³⁵S. J. Kline and S. K. Robinson, “Quasi-coherent structures in the turbulent boundary layer. Part 1: Status report on a community-wide summary of the data,” in *Near Wall Turbulence*, edited by S. J. Kline and N. H. Afgan (Hemisphere, New York, 1989), pp. 218–247.
- ³⁶R. J. Adrian, K. T. Christensen, and Z.-C. Liu, “Analysis and interpretation of instantaneous turbulent velocity fields,” *Exp. Fluids* **29**, 275 (2000).
- ³⁷P. Chakraborty, S. Balachandar, and R. J. Adrian, “On the relationships between local vortex identification schemes,” *J. Fluid Mech.* **535**, 189 (2005).
- ³⁸S. S. Lu and W. W. Willmarth, “Measurements of the structure of the Reynolds stress in a turbulent boundary layer,” *J. Fluid Mech.* **60**, 481 (1973).
- ³⁹R. J. Adrian, “Statistical properties of particle image velocimetry measurements in turbulent flow,” in *Laser Anemometry in Fluid Mechanics III* (Inst. Superior Tecnico, Ladoan, 1988), pp. 115–129.
- ⁴⁰R. J. Adrian, “Stochastic estimation of sub-grid scale motions,” *Appl. Mech. Rev.* **43**, 214 (1990).
- ⁴¹R. J. Adrian, P. Moin, and R. D. Moser, “Stochastic estimation of conditional eddies in turbulent channel flow,” in *CTR Proceedings of the Summer Program*, 1987, pp. 7–19.
- ⁴²R. J. Adrian, “Stochastic estimation of the structure of turbulent fields,” in *Eddy Structure Identification* (Springer, New York, 1996), pp. 145–196.